

1 **Kinetic-scale magnetic turbulence and finite Larmor** 2 **radius effects at Mercury**

V. M. Uritsky¹, J. A. Slavin², G. V. Khazanov², E. F. Donovan¹, S. A.

Boardsen², B. J. Anderson³, and H. Korth³

arXiv:1104.2618v1 [physics.space-ph] 13 Apr 2011

V. M. Uritsky, Physics and Astronomy Department, University of Calgary, SB605, 2500 University Drive NW, Calgary, AB T3A0P4, Canada. (uritsky@ucalgary.ca)

¹University of Calgary, Calgary, AB,
Canada

²NASA Goddard Space Flight Center,
Greenbelt, MD, USA

³John Hopkins University Applied
Physics Laboratory, Laurel, MD, USA

3 **Abstract.** We use a nonstationary generalization of the higher-order struc-
4 ture function technique to investigate statistical properties of the magnetic
5 field fluctuations recorded by MESSENGER spacecraft during its first flyby
6 (01/14/2008) through the near Mercury’s space environment, with the em-
7 phasis on key boundary regions participating in the solar wind – magneto-
8 sphere interaction. Our analysis shows, for the first time, that kinetic-scale
9 fluctuations play a significant role in the Mercury’s magnetosphere up to the
10 largest resolvable time scale (~ 20 s) imposed by the signal nonstationar-
11 ity, suggesting that turbulence at this planet is largely controlled by finite
12 Larmor radius effects. In particular, we report the presence of a highly tur-
13 bulent and extended foreshock system filled with packets of ULF oscillations,
14 broad-band intermittent fluctuations in the magnetosheath, ion-kinetic tur-
15 bulence in the central plasma sheet of Mercury’s magnetotail, and kinetic-
16 scale fluctuations in the inner current sheet encountered at the outbound (dawn-
17 side) magnetopause. Overall, our measurements indicate that the Hermean
18 magnetosphere, as well as the surrounding region, are strongly affected by
19 non-MHD effects introduced by finite sizes of cyclotron orbits of the consti-
20 tuting ion species. Physical mechanisms of these effects and their potentially
21 critical impact on the structure and dynamics of Mercury’s magnetic field
22 remain to be understood.

1. Introduction

23 Dynamic variability of Mercury’s magnetosphere has been intensively studied in the con-
24 text of tail and magnetopause reconnection, magnetic flux transport, ULF waves and oscil-
25 lations, and other phenomena (see e.g. *Anderson et al.* [2008]; *Slavin et al.* [2008, 2009a];
26 *Boardsen et al.* [2009a]; *Sundberg et al.* [2010]). However, little is known about mag-
27 netic turbulence in the Hermean plasma environment. *Korth et al.* [2010] investigated
28 turbulence in the unperturbed solar wind observed by MESSENGER at the heliocentric
29 distances of Mercury’s orbit, but they did not address magnetic fluctuations formed in
30 the vicinity of the planet. Considering the predicted significance of finite Larmor ra-
31 dius (FLR) effects and the abundance of plasma instabilities in Mercury’s magnetosphere
32 [*Glassmeier and Espley*, 2006; *Blomberg et al.*, 2007; *Travnicek et al.*, 2009], one can ex-
33 pect the magnetic fluctuations at this planet to be heavily affected by plasma kinetics.
34 This prediction, however, has not been tested on empirical data until now.

35 Turbulence in plasma is a fundamental physical phenomenon in its own right (see, for
36 instance, *Pouquet* [1978]; *Politano and Pouquet* [1995]; *Khazanov et al.* [1996]; *Robinson*
37 [1997]; *Biskamp* [2003]; *Mininni and Pouquet* [2007]; *Singh et al.* [2007]; *Schekochihin*
38 *et al.* [2009]). Large-scale stochastic plasma motions are controlled by the magnetohydro-
39 dynamic (MHD) energy cascade involving Alfvénic wave packets of various sizes which
40 tend to violate statistical laws derived for nonmagnetized fluids by exhibiting strong spa-
41 tial anisotropy [*Schekochihin et al.*, 2007]. In the resistive MHD approximation, the width
42 of the (inertial) range of scales defined by this regime is reflected by the magnetic Reynolds
43 number, with the main dissipation taking place at the distances shorter than the Taylor

44 microscale [*Uritsky et al.*, 2010a]. The situation is substantially more complicated in col-
45 lisionless plasmas with vanishing resistivity where the upper cutoff of the inertial range
46 in the wave-number space is created by ion kinetics. The latter usually generates a new
47 cascade with distinct physical and statistical properties, transferring the energy to even
48 smaller scales. Yet another type of turbulence is found at the electron scales as demon-
49 strated recently for the solar wind [*Sahraoui et al.*, 2009]. Understanding these effects is
50 an important problem with significant theoretical implications, including the fundamental
51 mechanisms of magnetic reconnection, particle acceleration and transport in space plas-
52 mas [*Chang*, 1999; *Lazarian and Vishniac*, 1999; *Antonova*, 2002; *Borovsky and Funsten*,
53 2003; *Uritsky et al.*, 2001; *Pulkkinen et al.*, 2006; *Uritsky et al.*, 2008; *Servidio et al.*, 2009;
54 *Eastwood et al.*, 2009; *Klimas et al.*, 2010].

55 In this study, we pursue a more practical goal by applying turbulent analysis tools as
56 a means of characterizing ion kinetic scales in different plasma structures surrounding
57 Mercury. Our methodology is based on the existence of scaling crossover separating
58 MHD and ion kinetic regimes of magnetic fluctuations. By identifying this crossover in
59 the temporal domain and mapping the results to the wave-number space using predicted
60 values of flow velocity, we evaluate the ion gyro radius and temperature in several locations
61 of the Hermean magnetosphere, and compare these measurements with earlier theoretical
62 estimates. We also show that scaling regimes of magnetic fluctuations vary greatly in
63 the Mercury's foreshock, magnetosheath, and the magnetosphere, and that they involve
64 contributions from a variety of non-random processes and structures, including boundary
65 layers, rotating flows, and transient ULF activity. Overall, our analysis suggests that ion
66 kinetic turbulence is present in all Hermean plasma structures, and is the leading source of

67 stochastic variability inside the magnetopause up to the largest resolvable scales imposed
68 by a data nonstationarity.

69 The paper has the following structure. The next section briefly summarizes properties of
70 magnetic fluctuations essential for this research, explains the link between the Fourier and
71 structure function analyses, and discusses several classes of turbulent cascades. Section 3
72 describes the methods and the data used in this study. One of the mathematical tools,
73 the continuous structure function scalogram, is introduced for the first time and to our
74 knowledge has not been used in space or turbulence studies before. In section 4, we present
75 the results of the analysis of magnetic fluctuations recorded during MESSENGER's first
76 flyby. We investigate nonstationary scaling structure of the these fluctuations and provide
77 comparative description of turbulent regimes in several key plasma regions visited by the
78 spacecraft. Finally, a summary of plasma parameters assessed using the measured ion
79 crossover scales is presented and discussed in the context of previous investigations.

2. Brief theoretical background

80 The autocorrelation properties of turbulent fluids are commonly described in frames of
81 two complementary statistical formalisms, the Fourier analysis and the structure function
82 approach (*Politano and Pouquet [1995]*).

The time-domain higher-order structure function (SF) is defined as

$$S_q(\tau) = \langle |\delta B_\tau|^q \rangle, \quad (1)$$

83 in which δB_τ are the increments of the studied turbulent field B measured at time lag τ ,
84 $\langle \cdot \rangle$ denotes averaging over all pairs of points separated by this lag, and q is the order. The
85 SF exponents ζ_q estimated from the scaling ansatz $S_q(\tau) \propto \tau^{\zeta_q}$, along with the spectral

86 exponent β describing the power-law decay of the wave-number Fourier power spectrum
 87 $P(k) \propto k^{-\beta}$, provide a detailed description of the turbulent regime under study. The
 88 second-order SF $S_2(\tau)$ plays a special role in statistical mechanics of turbulent media as
 89 a proxy to the band-integrated spectrum [*Biskamp, 2003*], yielding $\zeta_2 = \beta - 1$ under the
 90 assumption of linear space-time coupling as will be discussed later.

91 Fig. 1 illustrates the overall shape and mutual relationship between the wave-number
 92 Fourier power spectrum and the temporal SF for a typical turbulent environment observed
 93 by a spacecraft. Both statistical descriptions reveal three fundamental scaling regions
 94 labeled I through III in the Figure. Each region is characterized by its own set of power
 95 laws with distinct values of spectral and SF exponents.

96 The large-scale region I is dominated by MHD and hydrodynamic energy cascades
 97 represented by “fluid” exponent values $\beta \approx 1.5 - 2.0$ and $\zeta_2 \approx 0.5 - 1.0$. The frequently
 98 observed $\beta = 5/3$ ($\zeta_2 = 2/3$) corresponds to the Kolmogorov scaling of the Alfvén-wave
 99 energy spectrum of perpendicular wave modes indicative of a fully developed turbulent
 100 state [*Biskamp, 2003*]. The same 5/3 law describes the hierarchy of isotropic turbulent
 101 eddies in non-magnetic fluids [*Kolmogorov, 1941*]. As the wave number grows tending
 102 to the inverse ion gyro radius ρ_i^{-1} , plasma kinetics becomes increasingly important. For
 103 $k\rho_i < 1$ (or equivalently for $\tau > \tau_i$, where τ_i is the position of the ion crossover in
 104 the time-lag space), the kinetic effects can be treated by an extended MHD approach
 105 with kinetically-calculated anisotropic pressure tensor [*Schekochihin et al., 2007*]. In this
 106 sub-kinetic regime, the energy cascade continues to be supported by counter-propagating
 107 Alfvén wave packets, and the scaling exponents are approximately the same as in the
 108 usual MHD regime.

109 At the ion crossover scales $k\rho_i \sim 1$ and $\tau \sim \tau_i$, the kinetic MHD approximation breaks
 110 down since the Alfvénic fluctuations are no longer decoupled from the kinetic compo-
 111 nent of the turbulence represented by density and magnetic-field strength fluctuations
 112 [*Schekochihin et al.*, 2007]. The resulting scaling regime II, which will be referred to
 113 as the ion-kinetic regime throughout this paper, is characterized by the “ion” values of
 114 spectral and SF exponents which are larger than their fluid counterparts, leading to
 115 steeper log-log slopes of $P(k)$ and $S_q(\tau)$. The micro turbulence theories developed for this
 116 range of scales predict $\beta \approx 2.3 - 2.5$ (or $\zeta_2 \approx 1.3 - 1.5$), depending on the underlying
 117 dispersive wave mode (usually kinetic Alfvén waves (KAW) or whistler branches with
 118 secondary lower hybrid activity), and the turbulence type (i.e. a weak or strong), see
 119 e.g. *Yordanova et al.* [2008]; *Eastwood et al.* [2009]; *Sahraoui et al.* [2009]. Compressional
 120 corrections tend to increase the exponents [*Alexandrova et al.*, 2008] making them deviate
 121 further from fluid values.

122 As k reaches the inverse electron gyro radius ρ_e^{-1} (mapped to the time scale τ_e), both
 123 electrons and ions become demagnetized leading to a new scaling regime III with even
 124 higher β and ζ values. Physical mechanism of the electron cascade is currently not well
 125 understood, with oblique KAW modes being a candidate explanation for the cross-scale
 126 coupling in this regime [*Sahraoui et al.*, 2010].

127 Due to the collisionless dissipation at ion and electron gyroscales, only a certain fraction
 128 of the turbulent power in regions II and III arriving there from fluid scales is converted
 129 into turbulent cascades, while the rest is subject to Landau damping and other types
 130 of wave-particle interaction [*Khazanov*, 2010], steepening the apparent spectral and SF

131 slopes and making the kinetic-scale turbulence even more distinguishable from the fluid
132 regime.

3. Data and Methods

133 Keeping this theoretical framework in mind, we investigated time series of magnetic
134 field variations recorded by the MAG instrument [*Anderson et al.*, 2007] onboard the
135 MESSENGER spacecraft during its first flyby near Mercury (closest approach at 19:04:39
136 01/14/2008, sampling frequency 20 Hz). The northward direction of the interplanetary
137 magnetic field during this flyby provided ideal conditions for studying intrinsic properties
138 of Mercury’s magnetic fluctuations not distorted by a pronounced substorm activity. As
139 we show below, MESSENGER MAG is able to resolve the ion kinetic scales in all of the
140 Hermean plasma structures visited during the first flyby. The sampling frequency of MAG
141 is also sufficient for identifying these scales in the surrounding solar wind as demonstrated
142 by *Korth et al.* [2010].

143 Fig. 2 shows the trajectory of the spacecraft relative to the average positions of the
144 Mercury’s bow shock and magnetopause [*Slavin et al.*, 2009a]. Using the nonstationary
145 data analysis tools described below, we studied the evolution of magnetic turbulence
146 during the entire flyby, and performed a more focused investigation of selected plasma
147 regions discussed in previous publications [*Slavin et al.*, 2008, 2009a; *Boardsen et al.*,
148 2009a; *Sundberg et al.*, 2010]. These regions represent important boundary layers and
149 processes forming the response of Mercury’s magnetosphere to the solar wind driver.

150 The following regional identifiers are used throughout the paper: SW1 – unperturbed
151 solar wind at the dusk side; FS1 – outermost dusk-side foreshock region; FS2 – innermost
152 foreshock region near the dusk bow shock; MS1 – outermost magnetosheath at the dusk

153 flank; FTE – one-minute interval involving a flux transfer event [*Slavin et al.*, 2008]; MS2
 154 – innermost magnetosheath contacting the dusk magnetopause; KH – Kelvin - Helmholtz
 155 activity inside the dusk magnetopause [*Slavin et al.*, 2008; *Sundberg et al.*, 2010]; CCS –
 156 cross-tail current sheet; DD – first diamagnetic decrease encountered in the inner mag-
 157 netosphere; IBL – ion boundary layer adjacent to the dawn magnetopause [*Slavin et al.*,
 158 2008; *Anderson et al.*, 2011]; MS3 – innermost magnetosheath observed immediately after
 159 exiting dawn magnetopause; MS4 – outermost magnetosheath before crossing the dawn-
 160 side bow shock; FS3 – innermost foreshock region on the dawn side ; FS4 – outbound
 161 foreshock adjacent to the unperturbed solar wind; SW2 – solar wind observed at the end
 162 of the flyby. Timing information for each region is provided in Table 1. For the reader’s
 163 convenience, the regions are also marked by color-coded bars in Figs. 2 and 3.

164 To identify the ion crossover scales and other characteristic features of Mercury’s mag-
 165 netic turbulence, we used the method of higher order structure functions generalized for
 166 the case of strongly nonstationary signals.

167 Our choice of the SF-based approach to the magnetic turbulence at Mercury, as opposed
 168 to a somewhat more popular Fourier analysis, is motivated by two factors. First, SF
 169 analysis is a powerful tool of differentiating between random and deterministic components
 170 of multiscale variability. While the second-order SF contains essentially the same scaling
 171 information as the power spectrum (see Section 2), the other SF orders ($q \neq 2$) provide
 172 additional important clues on the structure of the studied signal; in particular, they enable
 173 identification of non-random transient disturbances mixed with stochastic noise. A purely
 174 random signal is described by the condition $\partial\zeta_q/\partial q > 0$, with the functional dependence
 175 of ζ on the order q quantifying the stochastic intermittency (“spikiness”) of the data

176 [*Politano and Pouquet, 1995*]. A set of “flat” SFs with $\zeta_q \approx 0 \forall q$ reveals the presence
 177 of singular features such as discontinuities and shocks. The inverted hierarchy of SF
 178 exponents ($\partial\zeta_q/\partial q < 0$) is indicative of a (quasi-) periodic wave oscillation embedded in
 179 a stochastic background, with the largest scale satisfying this criterion giving the period
 180 of the oscillation.

181 Secondly, the SF analysis is generally more robust when applied to nonstationary signals,
 182 as well as when the data amount is scarce. This advantage is crucial because MESSEN-
 183 GER’s magnetic measurements contain strong trends reflecting spatial inhomogeneity of
 184 the traversed plasma structures. Because of these trends, direct calculation of spectral
 185 power from a Fourier transform can be quite inaccurate, especially at the low frequencies
 186 comparable with the inverse time scale of the trends. Since the trends are nonlinear, de-
 187 trending the data introduces uncontrolled spectral errors and does not resolve the problem.
 188 SF analysis is much less sensitive to such effects and is statistically more stable when ap-
 189 plied to short data sets, the properties that are particularly useful for a windowed analysis
 190 of flyby time series.

191 The presence of scaling crossovers is usually evident in both the wave-number and the
 192 time-lag representations as illustrated by Fig. 1. However, the mapping between the
 193 crossover scales as seen in the k and τ domains depends on the state of the plasma and is
 194 not always straightforward. In the simplest case, when the bulk flow velocity v_0 is much
 195 higher than the characteristic propagation speed of the wave modes underlying turbulent
 196 motion, the Taylor “frozen-in flow” approximation $\omega = kv_0$ can be applied, which yields
 197 $k = 2\pi/v_0\tau$. By applying the ion-crossover condition $k\rho_i \approx 1$, we can therefore evaluate

198 the ion gyro radius and the ion temperature T_i (in energy units):

$$\rho_i \approx v_0 \tau_i / 2\pi, \quad (2)$$

$$T_i \approx m_i (v_0 \tau_i / \tau_{ci})^2, \quad (3)$$

199 in which τ_i is the ion crossover scale obtained from the temporal SF analysis, e_i and
 200 m_i are respectively the charge and the mass of the ions, $\tau_{ci} = 2\pi m_i / e_i B$ is the local
 201 gyroperiod, and B is the local magnetic field. The Taylor assumption used in these
 202 relations is approximately valid for the solar wind, the magnetosheath, the magnetopause
 203 boundary, and for the magnetotail plasma sheet [Matthaeus *et al.*, 2005; Alexandrova
 204 *et al.*, 2008; Yordanova *et al.*, 2008; Voros *et al.*, 2006]. For other magnetospheric regions,
 205 this assumption can be inapplicable and the space-time coupling far from trivial.

206 To deal with signal nonstationarity, we used the sliding window technique. The time
 207 series under investigation was segmented into a sequence of overlapping intervals of a
 208 fixed width Δ representing an empirical compromise between the nonstationarity and the
 209 intrinsic variability of the data, shifted by a constant shift $\Delta/2$. For each window position,
 210 we computed a set of SFs according to eq. 1 given in Section 2, with $q \in \{1, 2, 3, 4\}$ and
 211 $\tau < \Delta/2$.

The time-dependent shape of the resulting two-dimensional windowed structure function $S_q(\tau, t)$, with t being the running time variable given by the central position of the sliding window, was represented in two different formats: (1) by the time series $\zeta_q(t)$ of scaling exponents estimated over several selected τ ranges, and (2) as the continuous time – period scalogram $\zeta_q(\tau, t)$ enabling classification of turbulent regimes across the entire range of

available time scales:

$$\zeta_q(\tau, t) = \frac{\partial \log \left[\frac{1}{\Delta - \tau + 1} \sum_{t'=t-\Delta/2}^{t+\Delta/2-\tau} |\hat{B}(t') - \hat{B}(t' + \tau)|^q \right]}{\partial \log \tau}. \quad (4)$$

212 Here, $\hat{B}(t') = B(t') - \phi(t, t', \Delta)$ is the locally detrended magnetic signal, ϕ is the quadratic
 213 polynomial fit to the original signal B over windowed time interval $t' \in [t - \Delta/2, t + \Delta/2]$,
 214 and τ is the time scale not exceeding half of the window length Δ . The partial derivative
 215 in the above equation is evaluated from the local least-square linear regression slope of
 216 the $S_q(\tau)$ dependence in the log - log coordinates for each sliding window.

217 To our knowledge, the continuous scalogram technique defined by eq. (4) has not been
 218 used in space or turbulence studies before and is introduced in this paper for the first
 219 time.

220 In this work, we focus on the analysis of magnetic field modulus fluctuations ($B \equiv$
 221 $|B(t)|$) providing information on the spectrum of parallel fluctuations of the magnetic field.
 222 These fluctuations are known to be sensitive to ion kinetic effects above the ion spectral
 223 break $k\rho_i \sim 1$, and represent a distinctive signature of nonlinear compressible cascade
 224 [Alexandrova et al., 2008]. Anisotropic analysis of Mercury's magnetic turbulence, which
 225 will deliver a physically more accurate picture of ion-scale cascades in various Hermean
 226 regions, is left for future research.

4. Results and Discussion

4.1. Overview of scaling regimes

227 Fig. 3 presents the results of the windowed SF analysis of magnetic field fluctuations
 228 observed during the MESSENGER's first flyby. The studied signal (magnetic field mag-
 229 nitude) is shown on the top panel. The dashed (solid) vertical lines mark the times of

230 inbound and outbound crossings of the bow shock (magnetopause) boundaries positioned
 231 according to *Slavin et al.* [2008]. The dotted vertical lines show approximate locations
 232 of the outer foreshock boundary identified from our analysis. Upstream of this bound-
 233 ary, the magnetic fluctuations have a quasi-stationary structure of an ambient solar wind
 234 turbulence which is significantly perturbed inside the foreshock region.

235 Fig. 3(b) shows a stack plot of four time-dependent SF exponents ($q = 1 - 4$, window
 236 size $\Delta = 100$ s) as observed in several selected τ channels. During most of the time, the
 237 exponents obey the normal hierarchy with $\zeta_4 > \zeta_1$ characteristic of a stochastic noise.
 238 There are several noticeable excursions from this rule (marked by arrows) signaling the
 239 presence of transient ULF wave packets as discussed later in the text, the strongest one
 240 being the periodic oscillation in the τ channel 0.5-1.0 s detected soon after the closest
 241 approach [*Boardsen et al.*, 2009a, b].

242 The bottom panel (Fig. 3(c)) shows the second-order scalogram $\zeta_2(\tau, t)$ computed for
 243 the same magnetic signal. The local values of the ion crossover scale τ_i estimated from the
 244 condition $\zeta_2 \approx 1$ demarking the fluid and ion-kinetic ranges of magnetic turbulence (see
 245 Fig. 1) are plotted with the dashed-dotted line, along with the local proton gyro period
 246 (solid line). The scalogram confirms the existence of transient ULF wave activity (seen
 247 as pairs of vertically arranged red and blue spots) in several regions visited during the
 248 flyby. More importantly, it shows that the ion crossover scale undergoes a dramatic reor-
 249 ganization during the magnetospheric portion of the flyby, suggesting that even relatively
 250 large-scale plasma motions in this Hermean region should be affected by ion kinetics. To
 251 visualize this effect, the color coding in Fig. 3(c) is adjusted so that the “kinetic” range
 252 of values of the second-order SF exponent ($\zeta_2 > 1$) is painted in red and the “fluid” range

($0 < \zeta_2 < 1$) is in green. The red color clearly prevails inside the magnetospheric cavity. It can be seen that the interval of scales involved in the kinetic regime grows systematically as MESSENGER passes through the dusk magnetosheath, and it rapidly expands (by at least an order of magnitude) during the inbound magnetopause crossing. The outbound magnetopause crossing is accompanied by an abrupt decrease of τ_i . The ion crossover scale remains well above the local proton cyclotron period inside the magnetospheric cavity confirming the presence of strong FLR effects in the Mercury's magnetosphere, in agreement with numerous previous theoretical predictions (see e.g. *Glassmeier and Esp-ley* [2006]; *Delcourt et al.* [2007]; *Blomberg et al.* [2007]; *Travnicek et al.* [2009]; *Sundberg et al.* [2010] and refs. therein).

4.2. Comparative portraits of Hermean plasma structures

Fig. 4 shows the detailed shape results of second-order structure functions describing the magnetic turbulence in several key plasma regions visited by MESSENGER during its first flyby. The left (right) columns of plots represent the inbound (outbound) SF measurements. The discussion below follows the order in which plasma formations were traversed by the spacecraft.

Solar wind on both disk and dawn sides of Mercury exhibits classical signatures of large-scale fluid cascade coexisting with kinetic-scale turbulence. Some variability of low-frequency SF exponents seen in Fig.3(b) can be due to the inherent intermittency of the solar wind flow [*Roberts et al.*, 1992; *Borovsky*, 2010]. The structure functions have a crossover at $\tau \approx 0.5-1.0$ s (Fig. 4(a-b), black curves). The exponent above this scale is reasonably close to the Kolmogorov's law ($\beta = 5/3$, $\zeta_2 = 2/3$) in the outbound solar wind, and is more consistent with the Iroshnikov - Kraichnan scaling ansatz ($\beta = 3/2$, $\zeta_2 = 1/2$)

275 [*Biskamp*, 2003] in the outbound solar wind. For $\tau < 0.5$ s, the SF slopes are considerably
 276 steeper. The value $\zeta_2 > 1$ observed in this range of scales is indicative of the ion-kinetic
 277 regime, and it implies that the power spectral density of the magnetic fluctuations scales
 278 as $k^{-\beta}$ with $\beta \equiv \zeta_2 + 1 > 2$.

279 Compared to the inbound solar wind region (Fig.4(a)), the outbound solar wind mea-
 280 surements (panel (b)) are less stable, and they exhibit a more pronounced ion-kinetic
 281 component propagating toward larger τ , possibly reflecting wave turbulence initiated in
 282 the foreshock region upstream of the bow shock.

283 **The foreshock region** contains a strongly inhomogeneous turbulent environment filled
 284 with transient packets of quasi-periodic oscillations and high-frequency stochastic noise.
 285 During the inbound portion of the flyby, the solar wind structure undergoes an abrupt
 286 change at the upstream foreshock boundary which first affects the kinetic scales of the
 287 turbulent spectrum leaving the larger (MHD) scales almost unperturbed, see dashed red
 288 curve in Fig.4(a). After this magnetic fluctuations reorganize themselves across the entire
 289 τ range (solid red curve, same Figure). The repetitive decreases of short-scale SF expo-
 290 nents (marked with arrows in Fig.3(b)) indicate that the spacecraft has flown through
 291 several regions of ULF wave activity in both dusk- and dawn-side foreshocks as discussed
 292 above.

293 Our observations show that the Mercury's collisionless foreshock possesses a well-
 294 developed macrostructure possibly associated with ULF waves and discontinuities gen-
 295 erated by backstreaming ions [*Fairfield*, 1991; *Omidi et al.*, 2006]. Some of the detected
 296 intermittent structures can be due to hot flow anomalies upstream of the bow shock such
 297 as the ones found recently at Venus [*Slavin et al.*, 2009b]. Three-dimensional kinetic

simulations predict that the outbound foreshock may contain beams of plasma directed from Mercury's bow shock back upstream against the solar wind flow, resulting in a complex regime of wave-particle energy exchange manifested in long-wavelength beam-driven oscillations [Travnicek *et al.*, 2009].

The magnetosheath is dominated by intermittent kinetic fluctuations with nonlinear $\zeta(q)$ spectrum (not shown) converging to the ion-kinetic regime for $\tau \leq 1$ s, reminiscent of the turbulence in the terrestrial magnetosheath as observed by Cluster spacecraft [Yordanova *et al.*, 2008]. The stochastic component is mixed with transient episodes of ULF oscillations of various frequencies, the most intense ULF episode being observed in the inbound magnetosheath during 18:20-18:22 UT (shown by arrow in Fig. 3(b)) at a time scale of about one third of the local proton gyroperiod. The reorganization of magnetic fluctuations at the magnetosheath entry has begun from large scales (dashed blue curve in Fig. 4(c)) and involved shorter scales in about 15 minute after the inbound bow shock crossing. A fully-developed broad-band kinetic turbulence obtains in the near-magnetopause region of enhanced rms variability (solid blue curve, same panel). A similar sequence of events (in the reversed order) was observed while crossing the outbound bow shock (Fig. 4(d)) which also contains intense packets of ULF oscillations (Fig. 3 (b-c)).

Hybrid simulations show that downstream of the bow shock, Mercury's plasma is marginally stable with respect to mirror and cyclotron instabilities producing large-amplitude compressible waves [Travnicek *et al.*, 2009]. The same study suggests that the outbound magnetosheath can be also prone to fire-hose instabilities. It remains to be verified whether the ULF episodes present in our results for the Hermean magnetosheath are associated with some of these instability mechanisms.

321 During inbound magnetosheath observations, one flux transfer event (FTE) at
 322 UT=18:36:21-18:36:25 has been documented [*Slavin et al.*, 2008, 2010a]. FTEs in the
 323 magnetosheath are produced by localized magnetic reconnection between the interplane-
 324 tary and planetary magnetic fields, and are seen as passages of helical magnetic structures
 325 with a characteristic bipolar B_y signature encompassing a core region of an increased field
 326 magnitude. The magnetic fluctuations during the FTE (yellow curve in Fig. 2(c)) differ
 327 from those characterizing average conditions in the surrounding part of Mercury's mag-
 328 netosheath. Based on the shape of the second-order SF showing a nearly Kolmogorovian
 329 scaling, the FTE has launched a partly-developed fluid cascade modulated by a quasi-
 330 periodic distortion at $\tau \sim 4-6$ s consistent with the time scale of the bipolar B_y signature
 331 [*Slavin et al.*, 2008]. Our analysis also hints at the possibility of multiple FTEs and/or
 332 thin current sheets in the inbound magnetosheath during 18:24 - 18:37 UT (outlined by
 333 rectangle in Fig. 2(b)). Their presence is suggested by the anti-correlation between the
 334 SF exponents measured at $\tau = 5-15$ s and $\tau = 2.5-5$ s implying several transient features
 335 on a ~ 5 second time scale.

336 **Mercury's magnetosphere** reveals a rich diversity of scaling regimes most of which
 337 are shaped by kinetic-type fluctuations. The inbound magnetopause crossing is marked
 338 by a rapid transition from the magnetosheath turbulence characterized by relatively nar-
 339 row range of kinetic behavior, to a developed kinetic turbulence described by $\zeta_2 = 3/2$
 340 (indicative of ion-kinetic cascade [*Schekochihin et al.*, 2007]) over broad range of scales.
 341 The rather high upper time scale limit of ion-kinetic turbulence in the Kelvin-Helmholz
 342 instability region (Fig.4(2), dashed green line) matches the average period (~ 20 s) of vor-

343 tex rotations [Slavin *et al.*, 2008] and therefore does not necessarily represent an intrinsic
344 fluid crossover such as the one observed in the solar wind (Fig. 4(a)).

345 The equatorial plasma sheet (same panel, solid green line) displays ion-kinetic turbulent
346 scaling across the entire studied range of τ . This is quite different from the behavior of the
347 terrestrial current sheet outside the reconnection region. In the geotail, the dissipation
348 and kinetic effects usually play a leading role at $\tau < 1$ s while larger scales tend to be
349 controlled by an intermittent fluid cascade with $\beta < 2.5$ ($\zeta_2 < 1.5$), see Voros *et al.* [2006]
350 for a brief review. One can infer that the dynamics of the central plasma sheet in the
351 Hermean magnetosphere is strongly affected by non-MHD effects introduced by finite sizes
352 of cyclotron orbits of the constituting ion species, in agreement with earlier theoretical
353 predictions (see e.g. Delcourt *et al.* [2007]). As discussed in section 4.3, CCS turbulence
354 is consistent broadly with a very quiet, thick plasma sheet reported by Slavin *et al.* [2008]
355 based upon the large B_z magnetic field in the depressed equatorial tail and the northward
356 IMF B_z in the solar wind during the first flyby. The key open problem is the nature of
357 the waves in the dissipation range – whether the turbulent energy is deposited in the form
358 of kinetic Alfvén waves or whistler waves [Eastwood *et al.*, 2009]. Without simultaneous
359 electric and magnetic field measurements, this question may not have a definite answer.

360 The fluid component of the magnetospheric turbulence can be reliably identified only
361 during the near-Mercury portion of the flyby, namely during the first diamagnetic decrease
362 encountered in the inner magnetosphere [Slavin *et al.*, 2008], gray line in Fig. 4(f). Based
363 on the analysis of a similar region in the terrestrial magnetosphere [Uritsky *et al.*, 2010b;
364 Liu *et al.*, 2011; Panov *et al.*, 2010], these fluctuations can manifest transient velocity
365 and magnetic field shears due to reconnection - driven sunward flow bursts in the plasma

366 sheet. The flows are expected to stir turbulent vortices at the inner edge of the plasma
367 sheet where the sunward convecting plasma sheet ions encounter the stronger planetary
368 dipole magnetic field and are quickly decelerated [*Shiokawa et al.*, 1998]. At smaller radial
369 distances in the Earth’s magnetotail, fluid turbulence is suppressed due to a stabilizing
370 effect of the dipole magnetic field [*Stepanova et al.*, 2009, 2011]. A much weaker dipole
371 field at Mercury apparently allows turbulent vortices to penetrate closer to the planetary
372 surface.

373 Physical interpretation of the ULF wave activity observed after the closest approach
374 (see Fig. 3) remains a challenging task. Although the frequency of these waves is close to
375 the local proton gyro frequency, their mixed polarization, with a large amount of right-
376 hand polarized packets [*Boardsen et al.*, 2009a, b], does not fit the conventional picture
377 of ion-cyclotron resonant instability. A series of higher harmonics detected in the inner
378 magnetosphere during the first flyby suggests that the observed ULF oscillations may in
379 fact represent magnetosonic waves driven locally by a non-maxwellian proton distribution
380 [*Anderson et al.*, 2011].

381 The last (third) diamagnetic decrease traversed by MESSENGER before the outbound
382 magnetopause crossing demonstrates no signatures of fluid or MHD scaling (Fig. 4(f),
383 dashed orange line). The shape of the structure function of magnetic field modulus fluctu-
384 ations in this region is close to that in the first diamagnetic decrease. A more sophisticated
385 anisotropic analysis (to be published elsewhere) shows a distinct similarity between ra-
386 dial component of magnetic fluctuations in this region and at the adjacent magnetopause
387 boundary (solid blue line in Fig. 4(i)). This observation provides an indirect support to
388 the hypothesis by *Slavin et al.* [2008] who classified the third diamagnetic decrease as an

389 ion boundary layer compatible with the gyro-radius of sodium pickup ions accelerated in
390 the magnetosheath, and described this layer, together with the outbound magnetopause,
391 as an integrated double-magnetopause structure. On the other hand, simulations show
392 that temperature anisotropy in this region can be regulated by proton mirror and proton
393 cyclotron instabilities [Travnicek *et al.*, 2009]. Judging from the spectral amplitude of
394 magnetic fluctuations in the vicinity of proton gyro frequency [Anderson *et al.*, 2011],
395 kinetic effects in the IBL are likely to have much higher growth rates and/or saturation
396 levels than those in the inner magnetosphere. A proper kinetic treatment of the IBL region
397 involving a multi-ion plasma composition and accurate resolution of relevant instability
398 scales seems to be necessary for understanding the underlying physics of this complex
399 plasma structure.

400 The large-scale behavior of the SF plots presented in Fig. 4 enables an indirect verifica-
401 tion of the stationarity of the studied data segments. Following the approach proposed by
402 *Matthaeus and Goldstein* [1982], the stationarity of magnetic fluctuations can be tested
403 based on the ergodic theorem for stationary random processes [Monin and Yaglom, 1975].
404 In its simplest version, the theorem states that the time average of B obtained over
405 subintervals of a limited duration converges to the ensemble average as the length of the
406 subintervals significantly exceeds the correlation time of the signal. This condition en-
407 sures so-called weak stationarity of magnetic turbulence, and it tends to be fulfilled in
408 the interplanetary medium but not necessarily for planetary magnetic fluctuations. The
409 ergodic convergence poses a restriction on the asymptotic shape of the two-time autocor-
410 relation function $R(\tau)$ which must decay as τ^{-1} or faster (see *Matthaeus and Goldstein*
411 [1982] for details). It can be easily shown that this requirement is violated for $\zeta_2 > 1$

412 since in this case $R(\tau) \propto \tau^{-\alpha}$ with $\alpha = 2 - \zeta_2 < 1$ [Carreras *et al.*, 1999; Li, 2010], but
 413 is met for $\zeta_2 < 1$. The large-scale log-log slopes of all the plots in Fig. 4 are smaller
 414 than 1, and so the studied signals are stationarity at least in the weak sense. For some
 415 other locations in Mercury’s magnetosphere, however, the situation is not as clear. For
 416 instance, during the last two minutes (18:48-19:00) prior to entering the near-Mercury DD
 417 region, the crossover scale τ_i defined by the condition $\zeta_2 \approx 1$ was quite close to the upper
 418 measured time scale, see Fig. 3(c). This and similar regions require a more accurate
 419 stationarity analysis addressing convergence of higher statistical moments, and are not
 420 used for quantitative calculations in the Section 4.3 below.

421 For comparison purposes, Fig. 5 presents Fourier power spectra of magnetic turbulence
 422 in some of the magnetospheric regions discussed above. As expected, the shape of the
 423 spectra is consistent with the ion kinetic regime II (see Fig. 1) described by $\beta \approx 2.5$, but
 424 is statistically less stable than the shape of the SFs in the same range of scales (Fig. 4).
 425 The power spectra do not resolve the fine low-frequency structure of the studied signals
 426 which is clearly seen in the more robust structure function statistics. *Anderson et al.*
 427 [2011] have obtained Fourier power spectra of linearly detrended magnetic field data in
 428 the inner magnetosphere and in the IBL region. The spectral densities reported in their
 429 work undergo a rather steep decay characterized by $\beta \approx 2.5 - 3.0$ above the local proton
 430 cyclotron frequency, which is roughly consistent with the shape of the spectra in Fig. 5.

4.3. Quantitative estimates

431 Table 2 summarizes the results of our calculations of ion gyro radii and temperatures
 432 using eq.(2-3). The proton and sodium temperatures have been estimated assuming that
 433 the crossover scale τ_i is controlled by the gyromotion of protons and Na^+ ions, correspond-

434 ingly. We have considered only those plasma regions for which the Taylor frozen-in flow
 435 condition is roughly satisfied and so the linear mapping between the spatial and temporal
 436 domains of analysis is possible. As input parameters, we used the predicted values of bulk
 437 flow velocities for Hermean plasma environment [*Slavin et al.*, 2008; *Baker et al.*, 2009],
 438 the average flow velocity in a quiet Earth’s central plasma sheet [*Angelopoulos et al.*, 1993;
 439 *Baumjohann et al.*, 1989], as well as the values of the proton gyro period τ_{cp} and the ion
 440 crossover τ_i obtained from our analysis.

441 Solar wind parameters on the dusk (SW1) and dawn (SW2) sides of Mercury’s magne-
 442 tosphere are roughly consistent with the results of global solar wind simulations [*Baker*
 443 *et al.*, 2009, 2011] which predict $\rho_i \approx 18$ km and $T_p \approx 10$ eV for the first MESSEN-
 444 GER’s flyby. If we accept that τ_i in the solar wind is controlled by the ion inertial length
 445 $\lambda_i = c/\omega_{pi}$, where c is the speed of light and ω_{pi} is the ion plasma frequency, rather than
 446 by ρ_i (see *Sahraoui et al.* [2009] and *Sahraoui et al.* [2010] for details), the turbulence-
 447 based estimates become closer to the simulated values. For a plasma beta (the ratio of
 448 the particle pressure to magnetic pressure) of the order 1, this assumption yields $\rho_i \approx 20$
 449 (30) km, $T_p \approx 11$ (25) eV, and the proton number density $n_p \approx 65$ (40) cm^{-3} at the dusk
 450 (dawn) flanks. The inbound numbers are in a good agreement with *Baker et al.* [2009]
 451 as well as with typical solar wind parameters at Mercury orbit [*Blomberg et al.*, 2007].
 452 The outbound estimates reveal somewhat hotter plasma environment, possibly due to an
 453 extended quasi-parallel foreshock system existing at the dawn side.

454 The magnetosheath plasma estimates vary greatly with time and position as can be
 455 expected from the behavior of nonstationary ζ_q exponents and the SF scalogram con-
 456 structed for this region (Fig. 3). *Sundberg et al.* [2010] have reported a characteristic

457 proton temperature in the Mercury's magnetosheath of about 700 eV obtained by scaling
458 the terrestrial magnetosheath proton temperature with the scaling factor given in *Slavin*
459 *and Holzer* [1981]. Our temperature estimates for the inbound (MS2) and outbound
460 (MS3) magnetosheath regions adjacent to the magnetopause are significantly below this
461 predicted value. However, the proton temperature in many other magnetosheath locations
462 exceeds the prediction. For example, the flux transfer event in the dusk magnetosheath
463 is characterized by $T_p \approx 1200$ eV and the ion Larmor radius of ~ 240 km, or about 20%
464 of the size of the FTE as estimated by *Slavin et al.* [2008]. The flux rope topology of this
465 FTE should therefore be considerably affected by FLR effects.

466 Hybrid simulations of the first flyby [*Travnicek et al.*, 2009] demonstrate a steep in-
467 crease (by a factor of 3) in the ion temperature during the inbound magnetopause cross-
468 ing, accompanied by a noticeable drop in the plasma density. They also predict strong
469 temperature gradient at the dawn magnetopause. Both transitions are clearly present in
470 our results showing a sharp increase (decrease) of the estimated T_i and ρ_i values during
471 the inbound (outbound) magnetopause crossings. These transitions are also captured by
472 the dramatic growth of τ_i at the dusk boundary and the decay of the this parameter on
473 the dawn side (see Fig.3(c)).

474 The conditions at the magnetopause boundary suggest a significant contribution from
475 FLR effects, with the largest $\rho_i \sim 0.1R_M$ observed just inside the inbound magnetopause.
476 Due to final gyro orbits, the dusk side magnetopause can be either less stable than the
477 dawn magnetopause, or not stable at all [*Glassmeier and Espley*, 2006]. The pronounced
478 signatures of KH activity observed at the inbound magnetopause during the first flyby
479 confirmed the prediction [*Slavin et al.*, 2008; *Sundberg et al.*, 2010]. The possibility of

Kelvin - Helmholtz vortices on the opposite side of Mercury's magnetopause remains
 controversial. Using an FLR extension of the ideal MHD, *Glassmeier and Espley* [2006]
 have shown that the smallest KH-unstable wavenumber $\lambda_{min} = 8\pi\eta/|\delta v|$ at the dawn
 magnetopause is controlled by the the kinematic viscosity $\eta = \rho_i^2\omega_{ci}/4$ and the magnitude
 $|\delta v|$ of the velocity shear. Our measurements suggest that both the dusk and the dawn
 flanks of Mercury's magnetosphere can be prone to KH instability. By plugging the
 plasma parameters of dawn magnetopause (Table 2) into the above expressions, we obtain
 $\eta \sim 10^8 - 10^9$ m²/s and λ_{min} of the order of 100 km. This implies that the KH growth
 rate in this region can be positive for a wide range of wavenumbers, in agreement with
 recent theoretical results [*Sundberg et al.*, 2010].

The narrow-band ULF wave packets observed by MESSENGER between the closest
 approach and the outbound magnetopause [*Slavin et al.*, 2008] should be also strongly
 affected by finite gyro radii. The frequency of these waves has been found to be close
 to the local He⁺ cyclotron frequency [*Boardsen et al.*, 2009a, b], which is by an order of
 magnitude larger than the frequency corresponding to the ion crossover scale in this region
 ($\tau_i \sim 10$ s). The generation mechanism of these Hermean wave packets is very likely to be
 kinetic. The measured τ_i value is comparable with local cyclotron period of sodium ions
 (~ 20 s) hinting at their involvement in the cross-scale coupling processes in the studied
 magnetospheric region. This is quite different from Earth's magnetosphere where ULF
 waves tend to have frequencies well below all relevant gyro frequencies [*Blomberg et al.*,
 2007].

According to our investigation, the cross-tail current sheet (CCS) plasma population at
 Mercury can be significantly denser and cooler than the one typically observed at Earth.

503 The size of the gyro radius reported in Table 2 is also by a factor of two smaller than the
 504 one inferred from the measurements performed by MESSENGER Fast Imaging Plasma
 505 Spectrometer (FIPS) ($T_p \sim 2 \times 10^6$ K, or 170 eV, according to *Raines et al.* [2010]) which
 506 yield $\rho_i \sim 120$ km. Pressure-balance arguments [*Slavin et al.*, 2011] provide a current
 507 sheet plasma beta of ~ 5 for the studied flyby. Using this beta value, we obtain $n_p \sim 40$
 508 cm^{-3} , which exceeds FIPS estimates ($n_p \sim 1\text{-}10 \text{ cm}^{-3}$).

509 Our CCS results are not completely unexpected considering the northward IMF orien-
 510 tation during the studied time interval. A super-dense, cool plasma sheet material similar
 511 to the one reported here has been sighted in the terrestrial magnetosphere during extreme
 512 geomagnetic calm intervals characterized by steady northward IMF B_z (see *Borovsky and*
 513 *Steinberg* [2006] and refs therein). Such calm intervals may be important for precondi-
 514 tioning the magnetosphere for subsequent geomagnetic perturbations. Cool plasma can
 515 be an effective contributor to the inner magnetosphere since cool plasma sheet particles
 516 are less subject to gradient curvature drift and can be convected deeper into the dipole re-
 517 gion and therefore producing greater adiabatic pressure increase compared to hot particles
 518 [*Borovsky and Steinberg*, 2006].

519 By applying the simple $1/r^2$ correction (where r is the distance from the Sun, see
 520 *Ogilvie et al.* [1977]) to the proton densities of $\sim 3.0 - 4.5 \text{ cm}^{-3}$ reported by *Borovsky*
 521 *and Steinberg* [2006] for the dense terrestrial plasma sheet, we expect the corresponding
 522 Hermean values to be in the range $n_p \sim 30 - 50 \text{ cm}^{-3}$, which agrees with the CCS density
 523 measured in our study ($n_p \sim 40 \text{ cm}^{-3}$). *Mukai et al.* [2004] have extrapolated data-driven
 524 terrestrial plasma sheet models by *Terasawa et al.* [1997] and *Tsyganenko and Mukai*
 525 [2003] to account for the substantially different interplanetary environment at Mercury

526 and get a baseline for the plasma analyzer onboard the upcoming BepiColombo mission.
527 Using this empirical extrapolation, the solar wind density $\sim 65 \text{ cm}^{-3}$ translates into the
528 plasma sheet density of $\sim 1 - 20 \text{ cm}^{-3}$ (see Fig. 2(b) of *Mukai et al.* [2004]). The upper
529 limit of 20 cm^{-3} corresponds to the cold and dense state of the Hermean plasma sheet
530 and is comparable with our density estimate.

531 If the estimates provided in Table 2 are correct, the relatively small ion scales in the
532 Mercury's CCS could help explain the short characteristic substorm time scale of $\sim 1 - 3$
533 min [*Baumjohann et al.*, 2006; *Slavin et al.*, 2009c, 2011] on this planet. For Hermean
534 substorms to be this short, tail reconnection at Mercury has to be extremely fast and
535 intense [*Blomberg et al.*, 2007]. The reconnection rate is largely controlled by the current
536 sheet thickness which is of the order of the ion skin depth $\lambda_i \sim 35 \text{ km}$, based on our
537 assessment. For the convective inflow speeds of several hundreds kilometers per second,
538 the transition time of this depth would be a few 100 milliseconds. Furthermore, if the
539 reconnection at Mercury proceeds inside the ion diffusion region on electron inertial scale
540 which we estimate to be $\sim 1 \text{ km}$, the transition time could be as little as 10 ms, making
541 fast impulsive reconnection possible and perhaps inevitable.

542 In the absence of sufficiently intense tail lobe loading, no actual substorm activity was
543 observed during the studied flyby. In agreement with this fact, our analysis suggests
544 that proton trajectories in Mercury's current sheet were nearly adiabatic. The effects of
545 magnetic moment scattering in thin current sheets can be conveniently measured by the
546 adiabaticity parameter κ introduced by *Buchner and Zelenyi* [1989]. By definition, κ is
547 the square root of the ratio of the smallest field-of-line curvature radius to the largest ion
548 Larmor radius. For particles traveling through a field reversal, the condition $\kappa > 3$ ensures

549 adiabatic behavior; for $\kappa < 3$, the magnetic moment scattering is responsible for particle
 550 injection into the loss cone [Sergeev *et al.*, 1983], with a possibility of parametric “islands”
 551 of quasi-adiabatic behavior at very small κ values [Delcourt *et al.*, 2006]. Assuming that
 552 the field line curvature radius is of the order of $1 R_M = 2440$ km and that the measured
 553 ρ_i approximates the maximum relevant Larmor radius, we get $\kappa \approx 7$. The result is well
 554 above the transitional value $\kappa = 3$, and is a signature of adiabaticity. To unfreeze the
 555 magnetic flux and initiate reconnection, a much more stretched magnetotail configuration
 556 would be required. Such a configuration has been reached during the second and the third
 557 MESSENGER’s flybys which revealed a rather strong dayside and nightside reconnection
 558 activity accompanied by intense loading and unloading events [Slavin *et al.*, 2009c, 2010b].

559 One more indication of a stable state of the current sheet is its relatively low Reynolds
 560 number Re evaluated using $(Re)^{3/4} \sim L/\ell$ [Warhaft, 2002], where L and ℓ are the largest
 561 and the smallest scales of the inertial range cascade, respectively. In the CCS case, L is
 562 defined by the size of the flow channel of the radial convective plasma transport. In the
 563 terrestrial plasma sheet, L is about 10% of the width of the plasma sheet, or ~ 2 Earth
 564 radii [Nakamura *et al.*, 2004], $\ell \approx 50$ km, and so $Re \sim 1600$ [Voros *et al.*, 2006], which is
 565 indicative of a marginally stable regime at the edge of turbulence. At Mercury, due to a
 566 smaller planetary size, the estimated Reynolds number is much lower. If we assume that
 567 the BBF channel width at Mercury is also 10% of the width of the tail, then $L = 0.5R_M$
 568 in the Hermean magnetosphere. Alternatively, using the scaling factor of 8 given by the
 569 ratio of terrestrial to Hermean magnetospheric sizes in units of the respective planetary
 570 radii [Ogilvie *et al.*, 1977], one can argue that the flow channel of 2 Earth radii becomes
 571 $\sim 0.25R_M$ at Mercury. By using $L = 0.25 - 0.5R_M$ and substituting $\rho_i = 60$ km from

572 Table 2 as a proxy to ℓ , we arrive at $Re \approx 22 - 55$. This fairly small Reynolds number
573 suggests a predominantly laminar regime of plasma flow in the Hermean cross-tail current
574 sheet, consistent with the shape of the SF in this region (Fig. 4(e)) which reveals a rather
575 limited interval of scales of fluid cascade, if any at all.

5. Conclusion

576 We have presented the results of a first investigation of magnetic fluctuations in the
577 near-Mercury space environment. Our main findings can be summarized as follows:

578 (1) Turbulent conditions in the solar wind during the studied flyby were close to stan-
579 dard, with well-developed MHD and ion-kinetic components, consistent with the results
580 reported by *Korth et al.* [2010] for MESSENGER’s solar wind observations.

581 (2) Foreshock plasma at Mercury is populated with transient oscillatory perturbations
582 organized over large spatial distances. This macrostructure can be associated with magne-
583 tosonic waves and ULF plasma modes generated by field-aligned ion beams as proposed
584 earlier [*Omidi et al.*, 2006]. The low frequency fluctuations in the foreshock have no
585 obvious association with any known type turbulent cascade.

586 (3) The magnetosheath turbulence is dominated by intermittent kinetic-scale fluctu-
587 ations, in agreement with similar observations at Earth. Judging from a single FTE
588 observation in the magnetosheath, traveling flux ropes can be a source of enhanced low-
589 frequency turbulence in this plasma region.

590 (4) Turbulence in Mercury’s magnetosphere is strongly influenced by finite gyroradius
591 effects, with fluid-type energy cascades playing secondary or no part in most of the re-
592 gions inside the magnetospheric cavity, which supports earlier theoretical predictions and
593 simulation results.

594 (5) Stochastic properties of the central current sheet in Hermean magnetotail speak
595 in favor of its relatively stable global configuration consistent with the steady northward
596 IMF driving and the absence of noticeable substorm activity during the first flyby.

597 Overall, our results show, for the first time, that turbulence in the Hermean magneto-
598 sphere as well as in the surrounding space region is strongly affected by non-MHD effects
599 introduced by finite sizes of cyclotron orbits of the constituting ion species. We conclude
600 that kinetic effects may play a critically important role in the Mercury's magnetosphere up
601 to the largest resolvable time scale (~ 20 s) imposed by signal nonstationarity. However,
602 the prevalence of turbulence signatures of kinetic processes does not necessarily mean that
603 the latter are determining the structure of Mercury' magnetic field. Rather, our results
604 indicate that these kinetic processes need to be identified, and their potential influence on
605 Hermean magnetosphere need to be understood. A more sophisticated statistical analysis
606 addressing multiscale anisotropic properties of magnetic turbulence formed under differ-
607 ent solar wind driving conditions will be required to clarify physical mechanisms of these
608 effects and their influence on other Hermean processes such as e.g. a tail reconnection,
609 plasma transport, generation of field-aligned currents, and ULF wave activity. These and
610 related tasks outline a fruitful field of future research.

611 **Acknowledgments.** We thank M. Goldstein for helpful comments on the manuscript
612 and valuable methodological discussions. V.U. acknowledges the hospitality of the
613 NASA/Goddard's Heliophysics Science Division where this study was performed.

References

- 614 Alexandrova, O., V. Carbone, P. Veltri, and L. Sorriso-Valvo (2008), Small-scale energy
615 cascade of the solar wind turbulence, *Astrophysical J.*, *674*(2), 1153–1157.
- 616 Anderson, B. J., M. H. Acuna, D. A. Lohr, J. Scheifele, A. Raval, H. Korth, and J. A.
617 Slavin (2007), The Magnetometer instrument on MESSENGER, *Space Science Rev.*,
618 *131*(1-4), 417–450, doi:10.1007/s11214-007-9246-7.
- 619 Anderson, B. J., M. H. Acuna, H. Korth, M. E. Purucker, C. L. Johnson, J. A. Slavin,
620 S. C. Solomon, and R. L. McNutt (2008), The structure of Mercury’s magnetic field from
621 MESSENGER’s first flyby, *Science*, *321*(5885), 82–85, doi:10.1126/science.1159081.
- 622 Anderson, B. J., J. A. Slavin, H. Korth, S. A. Boardsen, T. H. Zurbuchen, J. M.
623 Raines, G. Gloekler, J. R. L. McNutt, and S. C. Solomon (2011), The dayside
624 magnetospheric boundary layer at Mercury, *Planetary Space Sci. [in press]*, doi:
625 10.1016/j.pss.2011.01.010.
- 626 Angelopoulos, V., et al. (1993), Characteristics of ion flow in the quiet state of the inner
627 plasma sheet, *Geophysical Research Lett.*, *20*(16), 1711–1714.
- 628 Antonova, E. E. (2002), Magnetostatic equilibrium and turbulent transport in earths
629 magnetosphere: A review of experimental observation data and theoretical approaches,
630 *Int. J. of Geomagnetism and Aeronomy*, *3*(2), 117–130.
- 631 Baker, D. N., D. Odstrcil, B. J. Anderson, et al. (2009), Space environment of mercury
632 at the time of the first MESSENGER flyby: Solar wind and interplanetary magnetic
633 field modeling of upstream conditions, *J. Geophysical Research*, *114*(A1), A10101, doi:
634 10.1029/2009JA014287.

- 635 Baker, D. N., D. Odstrcil, B. J. Anderson, et al. (2011), The space environment of mer-
636 cury at the times of the second and third MESSENGER flyby, *Planetary Space Sci.*
637 *[submitted]*.
- 638 Baumjohann, W., G. Paschmann, and C. A. Cattell (1989), Average plasma properties in
639 the central plasma sheet, *J. Geophysical Research – Space Phys.*, *94*(A6), 6597–6606.
- 640 Baumjohann, W., et al. (2006), The magnetosphere of Mercury and its solar wind en-
641 vironment: Open issues and scientific questions, *Advances in Space Research*, *38*(4),
642 604–609, doi:10.1016/j.asr.2005.05.117.
- 643 Biskamp, D. (2003), *Magnetohydrodynamic turbulence*, Cambridge Univ. Press.
- 644 Blomberg, L. G., J. A. Cumnok, K. H. Glassmeier, and R. A. Treuman (2007),
645 Plasma waves in the Hermean magnetosphere, *Space Science Rev.*, *132*, 575–591, doi:
646 10.1007/s11214-007-9282-3.
- 647 Boardsen, S. A., B. J. Anderson, M. H. Acuna, J. A. Slavin, H. Korth, and S. C. Solomon
648 (2009a), Narrow-band ultra-low-frequency wave observations by MESSENGER during
649 its January 2008 flyby through Mercury’s magnetosphere, *Geophysical Research Lett.*,
650 *36*(1), L01,104, doi:10.1029/2008GL036034.
- 651 Boardsen, S. A., J. A. Slavin, B. J. Anderson, et al. (2009b), Comparison of ultra-low-
652 frequency waves at Mercury under northward and southward IMF, *Geophysical Research*
653 *Lett.*, *36*, L18,106, doi:10.1029/2009GL039525.
- 654 Borovsky, J. E. (2010), Contribution of strong discontinuities to the power spectrum of the
655 solar wind, *Phys. Rev. Lett.*, *105*(11), 111,102, doi:10.1103/PhysRevLett.105.111102.
- 656 Borovsky, J. E., and H. O. Funsten (2003), MHD turbulence in the Earth’s plasma sheet:
657 dynamics, dissipation, and driving, *J. Geophysical Research– Space Phys.*, *108*(A7),

- 658 1284, doi:10.1029/2002JA009625.
- 659 Borovsky, J. E., and J. T. Steinberg (2006), The "calm before the storm" in
660 CIR/magnetosphere interactions: Occurrence statistics, solar wind statistics, and mag-
661 netospheric preconditioning, *J. Geophysical Research – Space Phys.*, *111*(A7), A07S10,
662 doi:10.1029/2005JA011397.
- 663 Buchner, J., and L. M. Zelenyi (1989), Regular and chaotic charged-particle motion in
664 magnetotail-like field reversals .1. basic theory of trapped motion, *J. Geophysical Re-*
665 *search – Space Phys.*, *94*(A9), 11,821–11,842.
- 666 Carreras, B. A., et al. (1999), Experimental evidence of long-range correlations and self-
667 similarity in plasma fluctuations, *Phys. Plasmas*, *6*(5), 1885–1892.
- 668 Chang, T. (1999), Self-organized criticality, multi-fractal spectra, sporadic localized recon-
669 nections and intermittent turbulence in the magnetotail, *Phys. Plasmas*, *6*(11), 4137–
670 4145.
- 671 Delcourt, D. C., H. V. Malova, and L. M. Zelenyi (2006), Quasi-adiabaticity in bifurcated
672 current sheets, *Geophysical Research Lett.*, *33*(6), L06,106, doi:10.1029/2005GL025463.
- 673 Delcourt, D. C., F. Leblanc, K. Seki, N. Terada, T. E. Moore, and M. C. Fok (2007), Ion
674 energization during substorms at Mercury, *Planetary Space Science*, *55*(11), 1502–1508,
675 doi:10.1016/j.pss.2006.11.026.
- 676 Eastwood, J. P., T. D. Phan, S. D. Bale, and A. Tjulin (2009), Observations of tur-
677 bulence generated by magnetic reconnection, *Phys. Rev. Lett.*, *102*(3), 035,001, doi:
678 10.1103/PhysRevLett.102.035001.
- 679 Fairfield, D. H. (1991), Solar-wind control of the size and shape of the magnetosphere, *J.*
680 *Geomagnetism Geoelectricity*, *43*, 117–127.

- 681 Glassmeier, K. H., and J. Espley (2006), ULF waves in planetary magnetospheres, *Mag-*
682 *netospheric ULF waves: Synthesis and New Directions*, 169, 341–359.
- 683 Khazanov, G. V. (2010), *Kinetic theory of the inner magnetospheric plasma*, Springer.
- 684 Khazanov, G. V., T. E. Moore, E. N. Krivorutsky, J. L. Horwitz, and M. W. Liemohn
685 (1996), Lower hybrid turbulence and ponderomotive force effects in space plasmas sub-
686 jected to large-amplitude low-frequency waves, *Geophysical Research Lett.*, 23(8), 797–
687 800.
- 688 Klimas, A., V. Uritsky, and E. Donovan (2010), Multiscale auroral emission statistics
689 as evidence of turbulent reconnection in Earth’s midtail plasma sheet, *J. Geophysical*
690 *Research – Space Phys.*, 115, A06,202, doi:10.1029/2009JA014995.
- 691 Kolmogorov, A. (1941), The local structure of turbulence in incompressible viscous fluid
692 for very large Reynolds numbers, *Dokl. Akad. Nauk SSSR*, 30, 299–303.
- 693 Korth, H., B. J. Anderson, T. H. Zurbuchen, J. A. Slavin, S. Perri, S. A. Boardsen, D. N.
694 Baker, S. C. Solomon, and R. L. McNutt, Jr. (2010), The interplanetary magnetic field
695 environment at Mercury’s orbit, *Planetary Space Sci.* [submitted].
- 696 Lazarian, A., and E. T. Vishniac (1999), Reconnection in a weakly stochastic field, *As-*
697 *trophysical J.*, 517(2), 700–718.
- 698 Li, M. (2010), Fractal time series - a tutorial review, *Math. Problems in Engineering*,
699 2010, 157,264, doi:doi:10.1155/2010/157264.
- 700 Liu, W. W., L. F. Morales, V. M. Uritsky, and P. Charboneau (2011), Formation and
701 disruption of current filaments in a flow-driven turbulent magnetosphere, *J. Geophysical*
702 *Research - Space Phys.*, 116, A03,213, doi:10.1029/2010JA016020.

- 703 Matthaeus, W. H., and M. L. Goldstein (1982), Stationarity of magnetohydrodynamic
704 fluctuations in the solar wind, *J. Geophysical Research – Space Phys.*, *87*(NA12), 347–
705 354.
- 706 Matthaeus, W. H., S. Dasso, J. M. Weygand, L. J. Milano, C. W. Smith, and M. G. Kivel-
707 son (2005), Spatial correlation of solar-wind turbulence from two-point measurements,
708 *Phys. Rev. Lett.*, *95*(23), 231,101.
- 709 Mininni, P. D., and A. Pouquet (2007), Energy spectra stemming from interac-
710 tions of alfvén waves and turbulent eddies, *Phys. Rev. Lett.*, *99*(25), 254,502, doi:
711 10.1103/PhysRevLett.99.254502.
- 712 Monin, A. S., and A. M. Yaglom (1975), *Statistical fluid mechanics: Mechanics of turbu-*
713 *lence*, vol. Vol. 2, MIT Press.
- 714 Mukai, T., K. Ogasawara, and Y. Saito (2004), An empirical model of the plasma envi-
715 ronment around Mercury, *Advances in Space Research*, *33*(12), 2166–2171.
- 716 Nakamura, R., et al. (2004), Spatial scale of high-speed flows in the plasma sheet observed
717 by Cluster, *Geophysical Research Lett.*, *31*(9), L09,804, doi:10.1029/2004GL019558.
- 718 Ogilvie, K. W., J. D. Scudder, V. M. Vasyliunas, R. E. Hartle, and G. L. Siscoe (1977),
719 Observations at planet Mercury by plasma electron experiment: Mariner 10, *J. Geo-*
720 *physical Research – Space Phys.*, *82*(13), 1807–1824.
- 721 Omidi, N., X. Blanco-Cano, C. T. Russel, and H. Karimabadi (2006), Global hybrid sim-
722 ulations of solar wind interaction with Mercury: Magnetospheric boundaries, *Advances*
723 *in Space Research*, *38*(4), 632–638, doi:10.1029/2008GL036630.
- 724 Panov, E. V., et al. (2010), Multiple overshoot and rebound of a bursty bulk flow, *Geo-*
725 *physical Research Lett.*, *37*, L08,103, doi:10.1029/2009GL041971.

- 726 Politano, H., and A. Pouquet (1995), Model of intermittency in magnetohydrodynamic
727 turbulence, *Phys. Rev. E*, *52*(1), 636–641.
- 728 Pouquet, A. (1978), 2-dimensional magnetohydrodynamic turbulence, *J. Fluid Mechanics*,
729 *88*(SEP), 1–16.
- 730 Pulkkinen, A., A. Klimas, D. Vassiliadis, and V. Uritsky (2006), Role of stochastic
731 fluctuations in the magnetosphere-ionosphere system: a stochastic model for the AE
732 index variations, *J. Geophysical Research – Space Phys.*, *111*(A10), A10,218, doi:
733 10.1029/2006JA011661.
- 734 Raines, J. M., J. A. Slavin, T. H. Zurbuchen, G. Gloeckler, B. J. Anderson, D. N. Baker,
735 H. Korth, S. M. Krimigis, and R. L. McNutt, Jr (2010), MESSENGER observations
736 of the plasma environment near Mercury, in *Abstracts of the 2010 Joint MESSENGER*
737 *BepiColombo workshop*, Boulder, CO.
- 738 Roberts, D. A., M. L. Goldstein, W. H. Matthaeus, and S. Ghosh (1992), Velocity shear
739 generation of solar wind turbulence, *J. Geophysical Research*, *97*(A11), 17,115–17,130.
- 740 Robinson, P. A. (1997), Nonlinear wave collapse and strong turbulence, *Rev. Modern*
741 *Phys.*, *69*(2), 507–573.
- 742 Sahraoui, F., M. L. Goldstein, P. Robert, and Y. V. Khotyaintsev (2009), Evidence of a
743 cascade and dissipation of solar-wind turbulence at the electron gyroscale, *Phys. Rev.*
744 *Lett.*, *102*(23), 231,102, doi:10.1103/PhysRevLett.102.231102.
- 745 Sahraoui, F., M. L. Goldstein, G. Belmont, P. Canu, and L. Rezeau (2010), Three dimen-
746 sional anisotropic k spectra of turbulence at subproton scales in the solar wind, *Phys.*
747 *Rev. Lett.*, *105*(13), 131,101.

- 748 Schekochihin, A. A., S. C. Cowley, and W. Dorland (2007), Interplanetary and inter-
749 stellar plasma turbulence, *Plasma Phys. Controlled Fusion*, *49*(5A), A195–A209, doi:
750 10.1088/0741-3335/49/5A/S16.
- 751 Schekochihin, A. A., S. C. Cowley, W. Dorland, G. W. Hammett, G. G. Howes,
752 E. Quataert, and T. Tatsuno (2009), Astrophysical gyrokinetics: kinetic and fluid tur-
753 bulent cascades in magnetized weakly collisional plasmas, *Astrophys. J. Suppl. Series*,
754 *182*(1), 310–377, doi:10.1088/0067-0049/182/1/310.
- 755 Sergeev, V. A., E. M. Sazhina, N. A. Tsyganenko, J. A. Lundblad, and F. Soraas (1983),
756 Pitch-angle scattering of energetic protons in the magnetotail current sheet as the dom-
757 inant source of their isotropic precipitation into the nightside ionosphere, *Planetary*
758 *Space Science*, *31*(10), 1147–1155.
- 759 Servidio, S., W. H. Matthaeus, M. A. Shay, P. A. Cassak, and P. Dmitruk (2009), Mag-
760 netic reconnection in two-dimensional magnetohydrodynamic turbulence., *Phys Rev*
761 *Lett*, *102*(11).
- 762 Shiokawa, K., et al. (1998), High-speed ion flow, substorm current wedge, and multiple
763 Pi 2 pulsations, *J. Geophysical Research - Space Phys.*, *103*(A3), 4491–4507.
- 764 Singh, N., G. Khazanov, and A. Mukhter (2007), Electrostatic wave generation and
765 transverse ion acceleration by Alfvénic wave components of broadband extremely low
766 frequency turbulence, *J. Geophysical Research - Space Phys.*, *112*(A6), A06,210, doi:
767 10.1029/2006JA011933.
- 768 Slavin, J. A., and R. E. Holzer (1981), Solar-wind flow about the terrestrial planets.
769 1 – Modeling bow shock position and shape, *J. Geophysical Research - Space Phys.*,
770 *86*(NA13), 1401–1418.

771 Slavin, J. A., M. H. Acuna, B. J. Anderson, et al. (2008), Mercury’s magnetosphere after
772 MESSENGER’s first flyby, *Science*, pp. 85–89.

773 Slavin, J. A., B. J. Anderson, T. H. Zurbuchen, et al. (2009a), MESSENGER observations
774 of Mercury’s magnetosphere during northward IMF, *Geophysical Research Lett.*, *36*,
775 L02101, doi:10.1029/2008GL036158.

776 Slavin, J. A., B. J. Anderson, D. N. Baker, et al. (2011), MESSENGER flyby observations
777 of Mercury’s magnetotail, *Planetary Space Sci.* [submitted].

778 Slavin, J. A., et al. (2009b), MESSENGER and Venus Express observations of the
779 solar wind interaction with Venus, *Geophysical Research Lett.*, *36*, L09,106, doi:
780 10.1029/2009GL037876.

781 Slavin, J. A., et al. (2009c), Messenger observations of magnetic reconnection in Mercury’s
782 magnetosphere, *Science*, *324*(5927), 606–610, doi:10.1126/science.1172011.

783 Slavin, J. A., et al. (2010a), MESSENGER observations of large flux transfer events at
784 Mercury, *Geophysical Research Lett.*, *37*, L02,105, doi:10.1029/2009GL041485.

785 Slavin, J. A., et al. (2010b), MESSENGER observations of extreme loading and unloading
786 of Mercury’s magnetic tail, *Science*, *329*(5992), 665–668, doi:10.1126/science.1188067.

787 Stepanova, M., E. E. Antonova, D. Paredes-Davis, I. L. Ovchinnikov, and Y. I. Yermolaev
788 (2009), Spatial variation of eddy-diffusion coefficients in the turbulent plasma sheet
789 during substorms, *Annales Geophysicae*, *27*(4), 1407–1411.

790 Stepanova, M., V. Pinto, J. A. Valdivia, and E. E. Antonova (2011), Spatial distribution
791 of the eddy diffusion coefficients in the plasma sheet during quiet time and substorms
792 from THEMIS satellite data, *J. Geophysical Research – Space Phys.*, *116*, A00I24.

- 793 Sundberg, T., S. A. Boardsen, J. A. Slavin, L. G. Blomberg, and H. Korth (2010),
794 The Kelvin-Helmholtz instability at Mercury: an assessment, *Planetary Space Science*,
795 *58*(11), 1434–1441, doi:10.1016/j.pss.2010.06.008.
- 796 Terasawa, T., et al. (1997), Solar wind control of density and temperature in the
797 near-Earth plasma sheet: WIND/GEOTAIL collaboration, *Geophysical Research Lett.*,
798 *24*(8), 935–938.
- 799 Travnicek, P. M., P. Hellinger, D. Schriver, D. Hercik, J. A. Slavin, and B. J. Anderson
800 (2009), Kinetic instabilities in Mercury’s magnetosphere: Three-dimensional simulation
801 results, *Geophysical Research Lett.*, *36*, L07104, doi:10.1029/2008GL036630.
- 802 Tsyganenko, N. A., and T. Mukai (2003), Tail plasma sheet models derived from
803 Geotail particle data, *J. Geophysical Research – Space Phys.*, *108*(A3), 1136, doi:
804 10.1029/2002JA009707.
- 805 Uritsky, V. M., A. J. Klimas, J. A. Valdivia, D. Vassiliadis, and D. N. Baker (2001),
806 Stable critical behavior and fast field annihilation in a magnetic field reversal model, *J.*
807 *Atmospheric Solar - Terrestrial Phys.*, *63*(13), 1425–1433.
- 808 Uritsky, V. M., E. Donovan, A. J. Klimas, and E. Spanswick (2008), Scale-free and scale-
809 dependent modes of energy release dynamics in the nighttime magnetosphere, *Geophys-*
810 *ical Research Lett.*, *35*(21), L21,101, doi:10.1029/2008GL035625.
- 811 Uritsky, V. M., A. Pouquet, D. Rosenberg, P. D. Mininni, and E. F. Donovan (2010a),
812 Structures in magnetohydrodynamic turbulence: Detection and scaling, *Phys. Rev. E*,
813 *82*(5), 056,326–1 – 056,326–15, doi:10.1103/PhysRevE.82.056326.
- 814 Uritsky, V. M., E. Spanswick, E. Donovan, J. Liang, J. Birn, D. Knudsen, and W. Liu
815 (2010b), Remote-sensing radial plasma flows in the magnetotail using multiscale vector

- 816 field techniques, *AGU Fall Meeting Abstracts*, pp. SM41A–1833.
- 817 Voros, Z., W. Baumjohann, R. Nakamura, M. Volwerk, and A. Runov (2006), Bursty
818 bulk flow driven turbulence in the Earth’s plasma sheet, *Space Science Rev.*, *122*(1-4),
819 301–311, doi:10.1007/s11214-006-6987-7.
- 820 Warhaft, Z. (2002), Turbulence in nature and in the laboratory, *Proc. National Acad.*
821 *Sciences United States Am.*, *99*, 2481–2486.
- 822 Yordanova, E., A. Vaivads, M. Andre, S. C. Buchert, and Z. Voros (2008), Magnetosheath
823 plasma turbulence and its spatiotemporal evolution as observed by the Cluster space-
824 craft, *Physical Review Letters*, *100*(205003), 205,003–1 – 4.

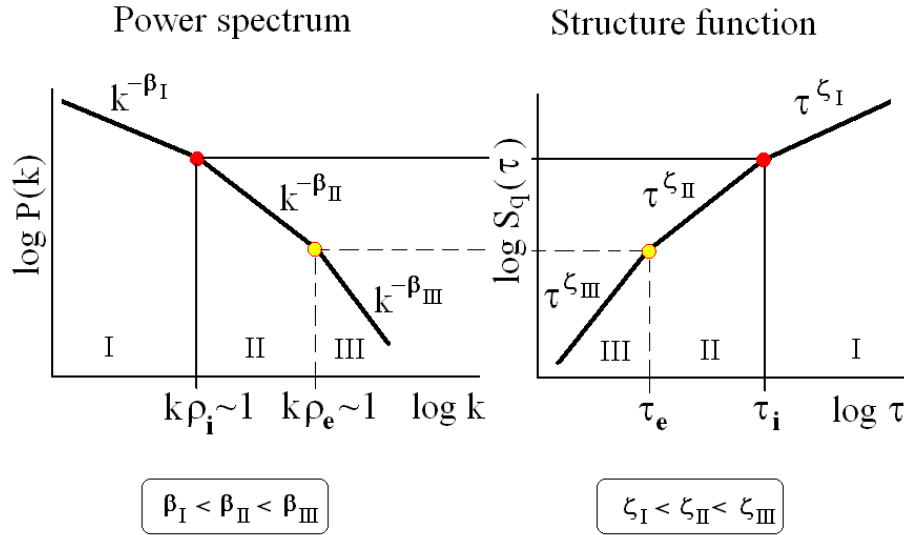


Figure 1. Schematic diagram showing the typical shape of the power spectrum and the structure function of magnetic turbulence involving abrupt changes (scaling crossovers) of the power-law exponents β and ζ at the ion and electron gyro scales. The hierarchy of the exponents in the fluid, ion- and electron-kinetic ranges of scales (regions I, II and III, correspondingly) is shown. The ion crossover characterized by $k\rho_i \sim 1$ is the main subject of this work.

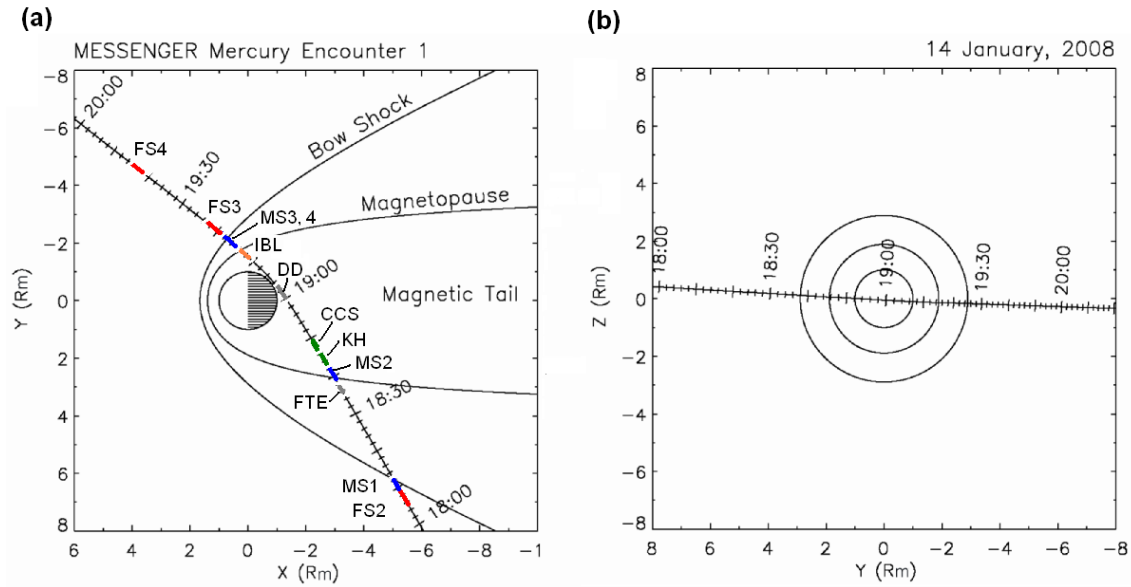


Figure 2. MESSENGER's first flyby trajectory overlapped with the average bow shock and magnetopause boundaries obtained using crossing information from five available flybys [Slavin *et al.*, 2009a]. Color bars show some of the studied regions, see Table 1 for full description.

Table 1. Intervals of analysis used for computing structure functions in Fig. 4–5.

Notation	Time	Description
SW1	17:10:00-17:40:00	Unperturbed solar wind at the dusk side
FS1	17:45:00-17:48:00	Outermost dusk-side foreshock region
FS2	18:05:30-18:08:30	Innermost foreshock region near the dusk-side bow shock
MS1	18:09:00-18:12:00	Outermost magnetosheath at the dusk flank
FTE	18:36:00-18:37:00	One-minute interval involving flux transfer event
MS2	18:39:00-18:42:00	Innermost magnetosheath contacting the inbound magnetopause
KH	18:43:00-18:46:00	Kelvin - Helmholtz vortices at the dusk magnetopause
CCS	18:47:00-18:49:00	Cross-tail current sheet
DD	19:00:00-19:03:00	First diamagnetic decrease encountered in the inner magnetosphere
IBL	19:11:00-19:14:00	Ion boundary layer adjacent to the outbound magnetopause
MS3	19:14:30-19:17:00	Innermost magnetosheath observed after exiting the magnetosphere
MS4	19:17:00-19:18:30	Outermost magnetosheath adjacent to the outbound bow shock
FS3	19:19:30-19:22:30	Innermost outbound foreshock region
FS4	19:42:00-19:45:00	Outbound foreshock adjacent to the unperturbed solar wind
SW2	19:52:00-20:22:00	Unperturbed solar wind at the dawn side

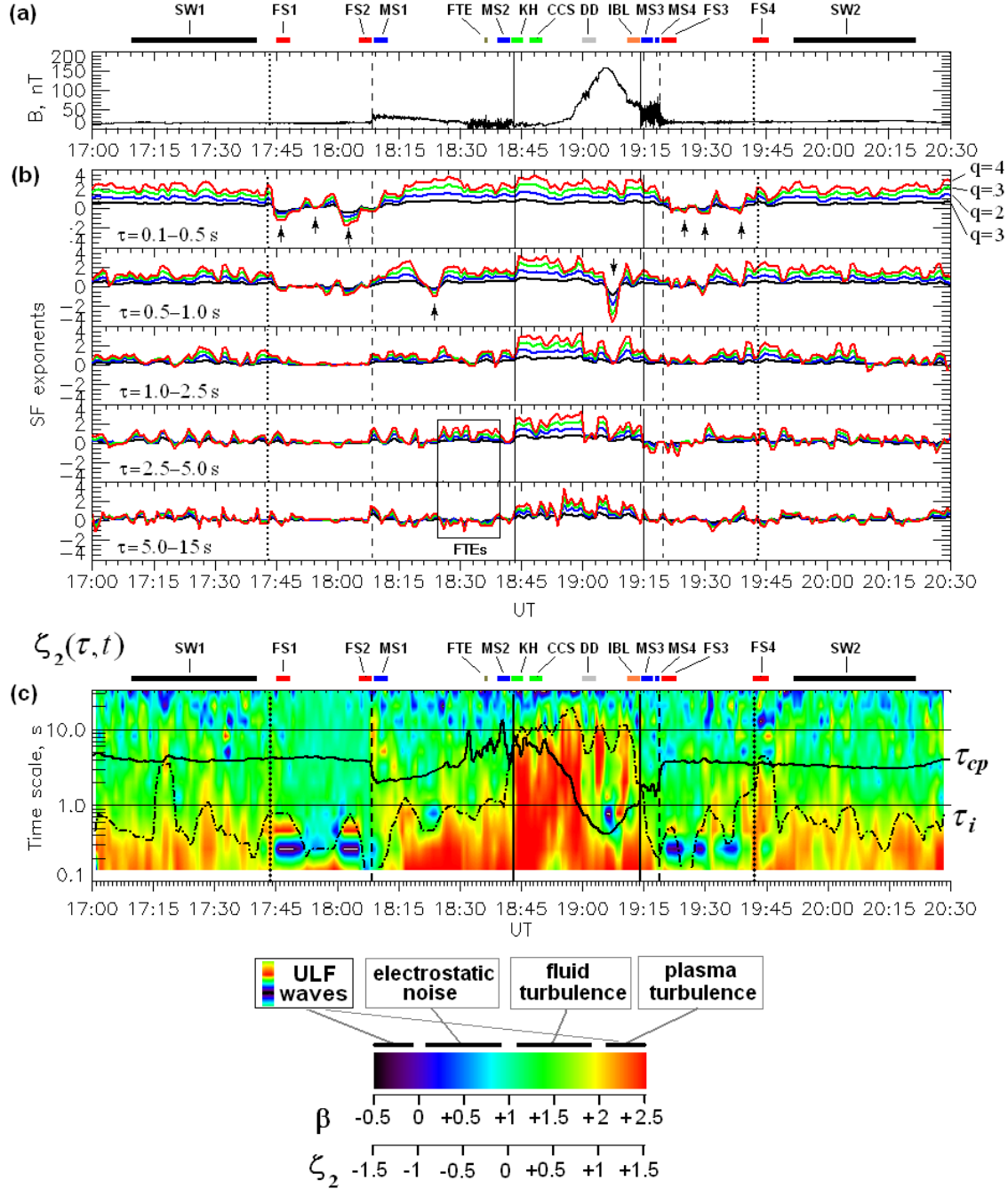


Figure 3. Windowed higher-order SF analysis of magnetic field fluctuations recorded during the first MESSENGER flyby. (a) Time series of the total field magnitude B . (b) Time-dependent structure function exponents (ζ_1 - black, ζ_2 - blue, ζ_3 - green, ζ_4 - red) estimated within five ranges of temporal scales of B variability. Black arrows show episodes of ULF activity discussed in the text. (c) Continuous second-order SF scalograms $\zeta_2(\tau, t)$ computed for the same signal. The red color corresponds to the fully developed ion-kinetic turbulent cascade with $\beta = 2.5$ and $\zeta_2 = 1.5$. Black solid line overlapped with the scalogram shows the local proton cyclotron period; dashed-dotted curve is an approximate ion crossover time scale evaluated from on the $\zeta_2 \approx 2$ condition using the SF analysis. The vertical solid, dashed, and dotted lines mark the inbound and outbound positions of the magnetopause, bow shock, and foreshock, correspondingly.

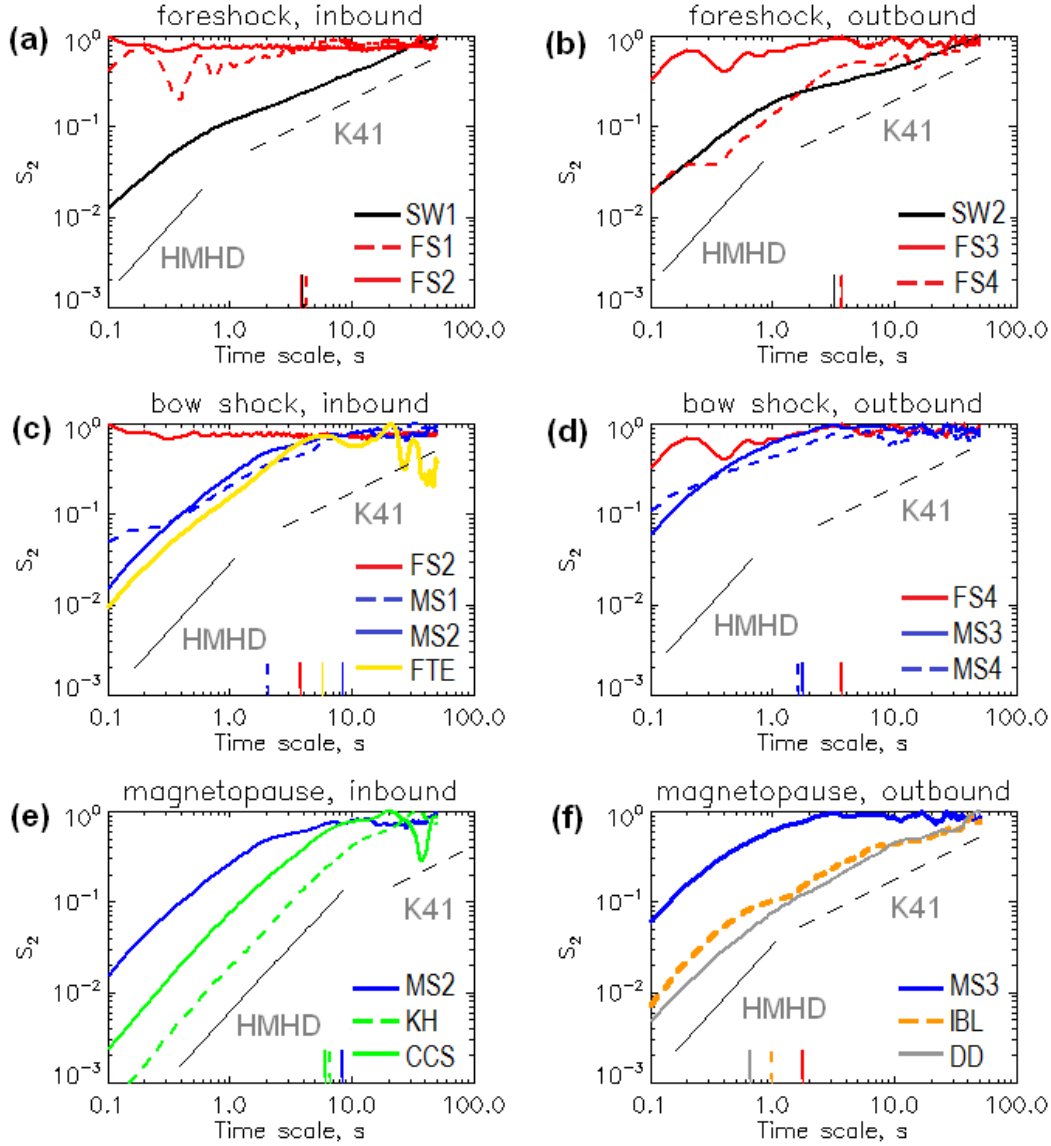


Figure 4. Second-order structure functions of magnetic field modulus fluctuations characterizing MESSENGER’s crossings of key Hermean plasma boundaries and structures. Left and right panels show inbound and outbound encounters, correspondingly. Proton cyclotron periods are shown with vertical lines of matching color and pattern on the bottom of each panel. Tilted straight lines representing theoretical slopes for the fully developed fluid (K41, $\zeta_2 = 2/3$) and Hall MHD (HMHD, $\zeta_2 = 3/2$) scaling regimes are added for reference to each plot. Notations and time limits of the studied regions are explained in Table. 1.

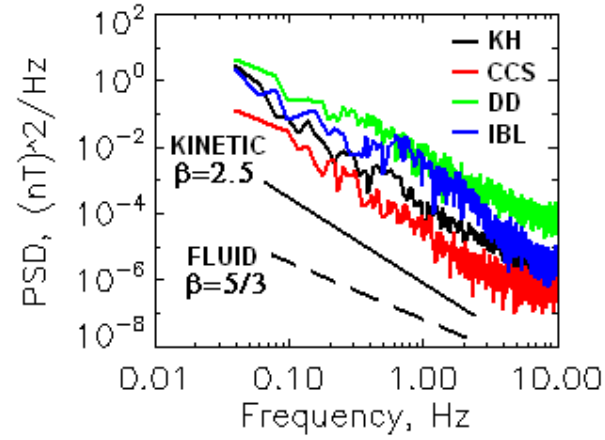


Figure 5. Fourier power spectra of several magnetospheric regions showing broad-band kinetic fluctuations consistent with Hall MHD interpretation. The spectral power law index β is related with the second-order SF exponent as $\beta = \zeta_2 + 1$.

Table 2. Estimated plasma parameters in selected regions of Hermean magnetosphere: τ_{cp} – proton cyclotron period; v_0 – typical bulk fluid velocity; τ_i – ion crossover scale corresponding to the transition between the fluid- and kinetic-like behavior of the structure function; ρ_i – ion gyroradius obtained using eq.(2); T_p (T_{Na}) – temperature of protons (Na^+ ions) evaluated from (3); $R_M \approx 2440$ km – radius of Mercury. See Table 1 for region notations.

Region	τ_{cp} , s	v_0 , km/s	τ_i , s	ρ_i , km	ρ_i/R_M	T_p , eV	T_{Na} , eV
SW1	3.9	450	0.4	30	0.01	25	–
FTE	4.6	300	5.0	240	0.10	1200	50
MS2	5.5	300	1.5	70	0.03	75	3
KH	5.9	150	10.0	240	0.10	700	30
CCS	6.0	50	7.0	60	0.03	40	2
IBL	1.0	150	3.0	70	0.03	2300	100
MS3	1.6	300	0.4	20	0.01	60	3
SW2	3.2	450	0.5	35	0.01	55	–
